Adaptive Optics in Multiphoton Microscopy

by

Aidyn Kemeldinov

Department of Physics
Duke University

Date:_____

Approved:

_____

Warren S. Warren, Supervisor

_____

Martin C. Fischer

_____

Stephen Teitsworth

Thesis submitted in partial fulfillment of
the requirements for the degree of
Master of Science in the Department of
Physics in the Graduate School
of Duke University

2017

ABSTRACT

Adaptive Optics in Multiphoton Microscopy

by

Aidyn Kemeldinov

Department of Physics
Duke University

Date:_____

Approved:

_____
Warren S. Warren, Supervisor

_____
Martin C. Fischer

_____
Stephen Teitsworth

An abstract of a thesis submitted in partial fulfillment of the requirements for the degree of Master of Science in the Department of Physics in the Graduate School of Duke University

2017

Abstract

Any type of microscopy faces the problem in an attenuated signal level and reduced optical resolution due to optical aberration. To overcome this problem, adaptive optics was implemented in a two-photon fluorescence microscope. Using a "sensorless" approach, this study corrected the aberration in the system using two different excitation colors. As methodology, the point spread function was compared before and after applying adaptive optics. This study demonstrated that adaptive optics improves the resolution of the microscope for both excitation wavelengths. The aberration correction was then monitored as a function of depth. The result showed an improvement in the optimization metric as imaging depth is increased. Thus, adaptive optics offers improved imaging of the sample at deeper depths with better optical resolution and higher signal-to-noise ratio.

Dedication

I dedicate this thesis to my soulmate, Aibope, for her unconditional love and support.

Contents

List of Tables

List of Figures

1. Introduction

In this chapter, the goal is to provide a general overview of some aspects of optical imaging. Different modalities of optical imaging are considered followed by the effects of aberration on optical imaging. Finally, I present some of the key physical concepts in adaptive optics and the application of adaptive optics in microscopy. Readers can find more rigorous details about the subjects in References [1-3].

1.1 Imaging Techniques

A microscope has been an important imaging tool for more than a century. Over the years, the developments in technology have expanded capabilities of a microscope. Confocal microscopy [4] is the breakthrough invention due to its ability to provide a three-dimensional image of the specimen with the use of a spatial filter to eliminate out-of-focus signals generated throughout the sample due to linear excitation [5]. The invention of ultrashort pulsed laser with high peak intensity at low average power has provided an opportunity to access multiphoton processes in microscopy. Two-photon excitation microscopy is a multiphoton imaging technique [6] which has emerged with several advantages over confocal microscopy due to its inherent optical sectioning capability. The generated signal in two-photon microscopy has a quadratic dependence on intensity and this signal is predominantly confined where intensity is highest, at the

focal plane, as shown in Figure 1. In two-photon microscopy, the same excitation as in confocal microscopy with a single photon, is produced with the simultaneous absorption of two photons with half energy of the single photon.

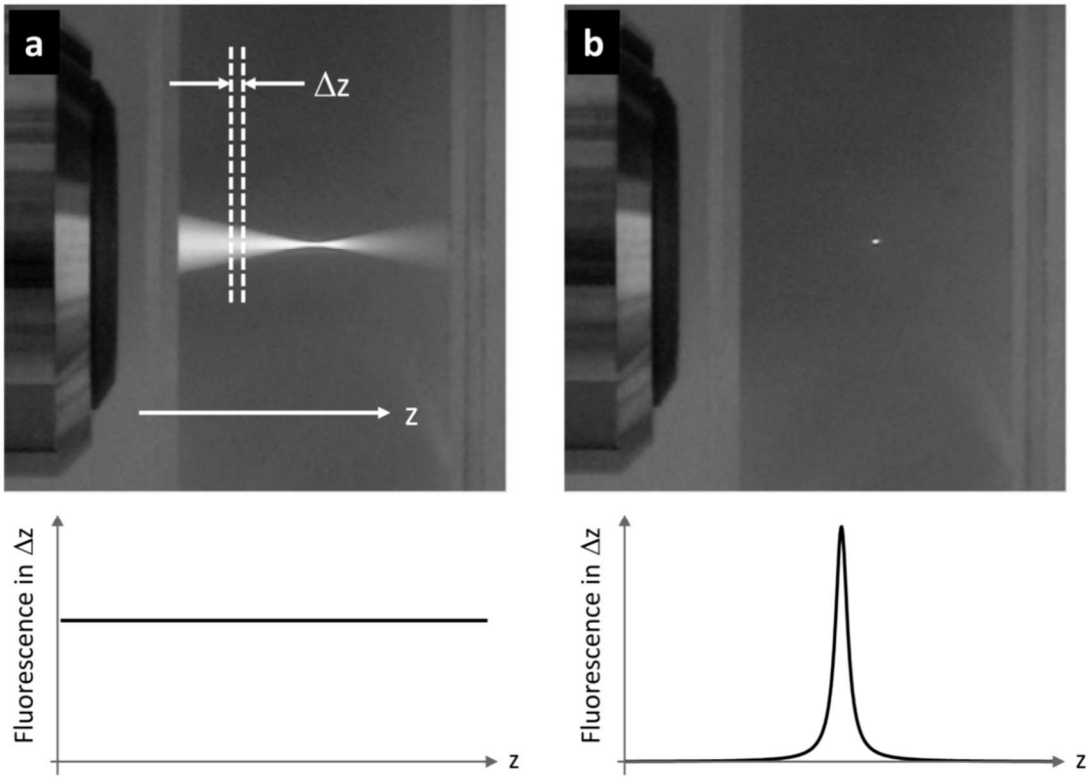

Figure 1: (Top) (a) continuous wave UV light and (b) short near-IR pulses generates fluorescence in R6G. (Bottom) Integrated fluorescence from a thin slice for (a) one-photon excitation and (b) two-photon excitation. Adapted from [3]

The utilization of the longer excitation wavelength provides reduced photodamage to the sample and reduced scattering within the sample; thus, two-photon microscopy provides greater penetration depth than confocal microscopy. However, two-photon fluorescence microscopy contrast requires the presence of fluorescence which limits the

range of available targets. Apart from two-photon microscopy, other nonlinear modalities, such as SHG [7, 8], THG [9, 10] and Coherent anti-Stokes Raman scattering (CARS) [11] have been developed to access to more diverse imaging targets.

Harmonic generation is a coherent non-linear process where two or more photons with the same energy are scattered to generate a single photon with the sum frequency of the incident photons. Because the SHG signal is associated with a second-order susceptibility, SHG provides contrast only when molecules possess non-centrosymmetric geometry, for example, collagen fibers [12] or microtubuli [13], whereas the THG signal is associated with a third-order susceptibility and it has been used in imaging at interface [14].

In Coherent anti-Stokes Raman scattering (CARS), two beams, called "pump" and "Stokes", produces the signal at the Anti-Stokes frequency when a beat frequency between "pump" and "Stokes" beams matches the Raman resonance of a molecule. CARS provides highly specific molecular contrast due to its sensitivity to molecular vibrational states. The application of CARS has been demonstrated in biological imaging studies [11].

As shown in Figure 2, image contrast for the aforementioned modalities, including two-photon excitation, is based on the generation of a new color. For some

imaging targets, the generation of a new color does not provide convenient imaging contrast since it does not possess a distinguished feature about the sample [3].

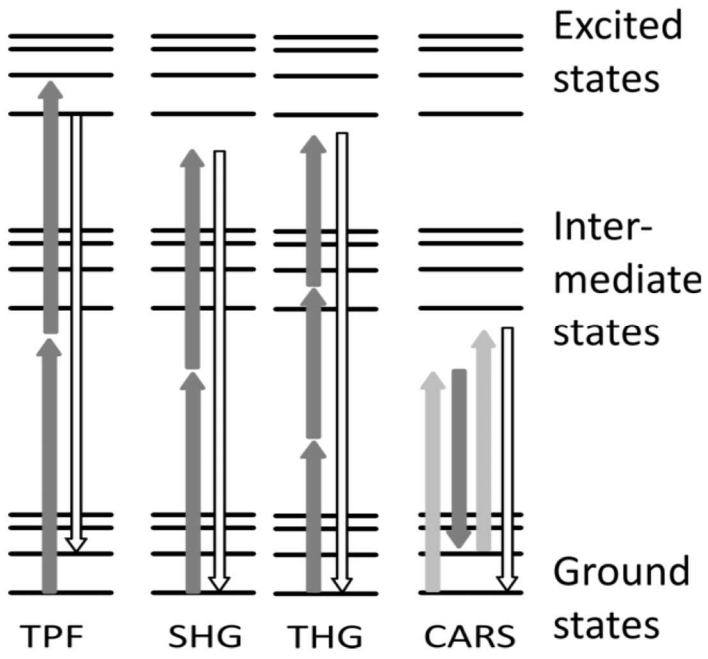

Figure 2: Nonlinear Interaction based on the generation of a new color. TPF (Two-photon fluorescence), SHG (Second-Harmonic Generation), THG (Third-Harmonic Generation) and CARS (Coherent Anti-Stokes Raman Scattering). Adapted from [3]

On the other hand, pump-probe microscopy, a time-resolved nonlinear microscopy, can provide image contrast without the generation of a new wavelength with great specificity about the molecular and morphological information of the sample [3]. Pump-probe measurement requires two ultrashort pulse trains, called "pump" and "probe". In the experiment, the excited state dynamics of a molecule is monitored by detecting imposed pump modulation on the probe beam. The image contrast is based on different

types of nonlinear optical interactions as shown in Figure 3. The application of pump-probe microscopy has been demonstrated in non-invasive imaging of biological samples [15, 16]. Additionally, this microscopy provides a method of non-destructive imaging of historical paintings [17].

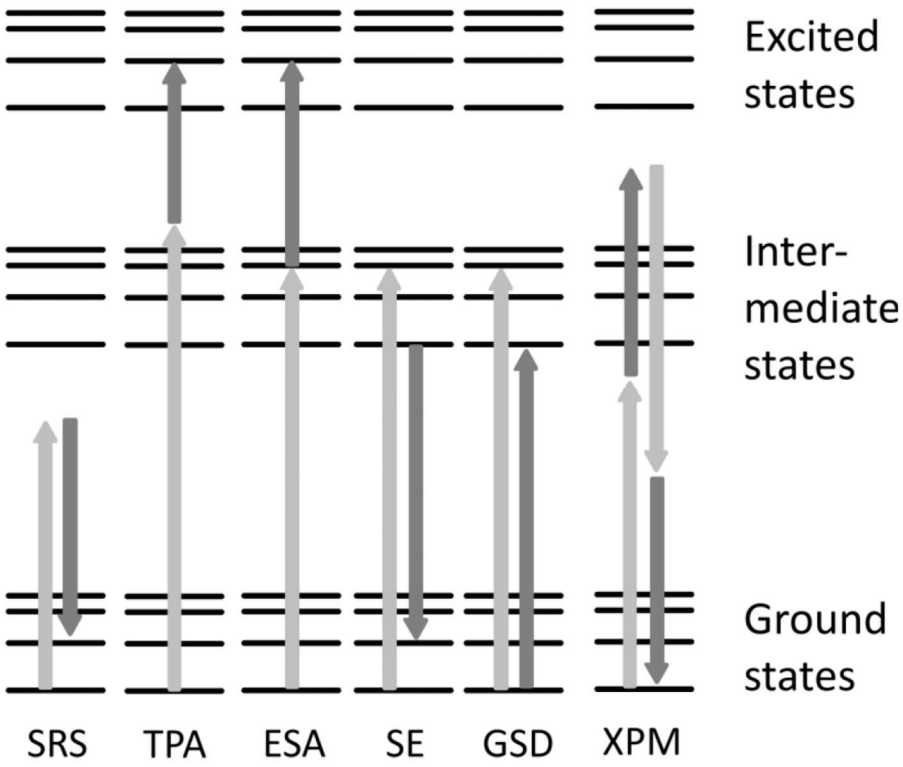

Figure 3: Nonlinear interactions that do not generate a new color. Stimulated Raman scattering (SRS), two-photon absorption (TPA), excited-state absorption (ESA), stimulated emission (SE), ground state depletion (GSD), and cross-phase modulation (XPM). Adapted from [3]

Nonetheless, any type of microscopy has limitations in a reduced signal level and reduced optical resolution in deeper imaging depth. One of the cause is an enlarged

focal excitation volume due to aberrated wavefront as it is shown in Figure 4. Thus, any optimization to reduce aberrations to operate close to the diffraction limit significantly improves the image contrast, the spatial resolution and the signal-to-noise ratio in a microscope [2].

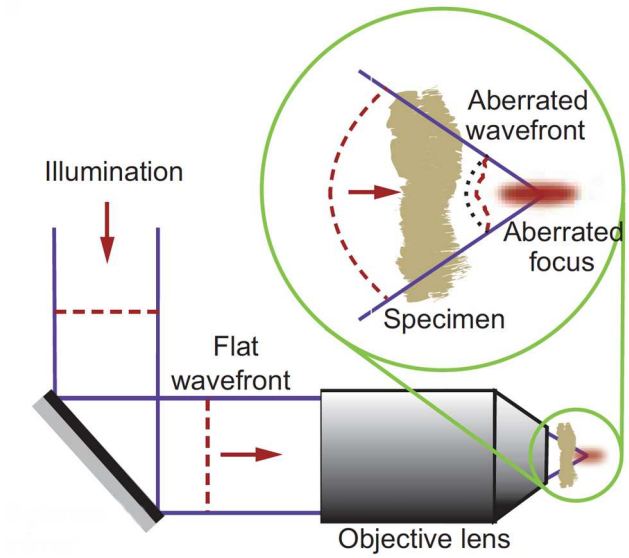

Figure 4: Effect of aberration on the imaging system. Aberrated wavefront leads to an enlarged focal point. Adapted from [2]

.

1.2 Theory of Image Formation

Under the paraxial approximation, let us consider the point spread function (PSF) of a lens which describes the imaging properties of the system and discuss the effects of aberration on the performance of a microscope.

Suppose, a lens with $NA = nsin(\alpha)$ is illuminated with a uniform plane wave. We can express the pupil function, the distribution of the phase and amplitude across the pupil plane of the lens, as:

$$P(\zeta, \eta) = \exp(i\psi(\zeta, \eta)) \qquad (1)$$

where $\psi(\zeta, \eta)$ is the phase function in the pupil plane, $\zeta = \rho cos\theta$ and $\eta = \rho sin\theta$ are related to the polar coordinates (ρ, θ). The phase function includes information about the size of the lens and aberration. The intensity PSF of the lens is then expressed:

$$I(t, w, u) = \left|\left(\int_{-1}^{1}\int_{-1}^{1} P(\zeta, \eta)\exp[i\frac{u}{2}(\zeta^2 + \eta^2) - i\,(\zeta t + \eta w)]d\zeta d\eta\right)\right|^2 \qquad (2)$$

where $u = \frac{8\pi}{\lambda} znsin^2\left(\frac{\alpha}{2}\right)$ is the normalized axial coordinate, $t = \frac{2\pi}{\lambda} xnsin\alpha$ and $w = \frac{2\pi}{\lambda} ynsin\alpha$ are the normalized lateral coordinates related to the Cartesian coordinates (x, y, z). Aberration introduces distortion on the phase function; thus, it affects the PSF of the lens. In spatial frequency domain, the aberration alters high-frequency components of the optical transfer function (OTF) and reduce the effective cut-off frequency of the imaging system [18]. As a result, the wavefront distortions spatially broaden the point spread function (PSF) and degrade the spatial resolution of the system.

1.3 Sources of Aberration

Let us now briefly discuss two main sources of optical aberration in microscopy: system-induced and sample-induced.

The former arises from imperfections in optical alignment, or when the system is operated outside of its designed configuration. For example, slight off-axis misalignment of a lens introduces known aberrations, such as astigmatism and coma [19]. Also, an incorrect configuration of the objective and the designed tube length can produce spherical aberration in the system [19].

The second source of aberration is induced by the spatial variation of the refractive index of the specimen which leads to decrease in signal intensity by enlarging a focal spot (Figure 4) and degrade the resolution of the system. Additionally, aberration could be caused by an index of refraction mismatch between the specimen and the immersion medium which induces spherical aberration [2]. One of the approaches to compensate the optical aberration in microscopy is implementing adaptive optics, a method successfully deployed in astronomy.

1.4 Adaptive Optics

Adaptive optics is the well-studied approach in astronomy to compensate optical aberration induced by atmospheric distortions and to restore the optimum resolution of the imaging system. For the first time the AO system was deployed for military purposes [20], although the concept was originally proposed by Horace Babcock twenty years earlier [21]. In astronomy, the basic adaptive optics systems consist of a wavefront corrector, a wavefront sensor and a feedback controller. As illustrated in Figure 5, light

from a telescope is captured and is reflected off a wavefront corrector (a deformable mirror). A wavefront sensor is then fed with a portion of reflected light from the deformable mirror to measure wavefront distortion. Using the signal from the wavefront sensor, a feedback controller reshapes the surface of the wavefront corrector to compensate wavefront aberration. However, it should be emphasized that some factors play a crucial role to optimally operate adaptive optics in astronomy. The most important one is the requirement of a reference point source near the imaging object to correctly measure wavefront distortion. Fortunately, there is a well-known approach to satisfy this condition by creating artificial "guide stars" close to the object by exciting sodium atoms in the mesosphere with a laser source.

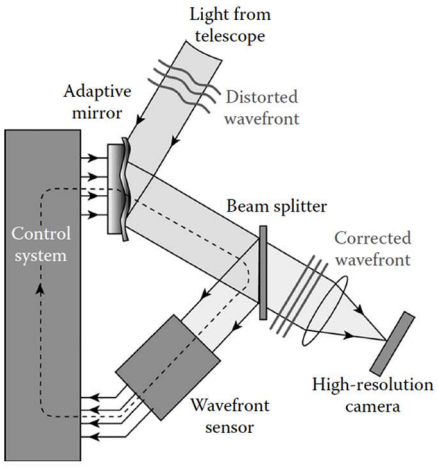

Figure 5: Adaptive optics system in astronomy. Light from an object is imaged onto an adaptive mirror. A portion of reflected light is directed to a wavefront sensor. A wavefront distortion is measured and using a control system the surface of the adaptive mirror is reshaped to correct the aberration. The corrected wavefront is imaged into a camera. Adapted from [1].

1.4.1 Wavefront correctors

Most of wavefront correctors fall into two categories: a deformable mirror and a spatial light modulator. Principle of operation to correct wavefront aberration for each type is shown in Figure 6 and 7.

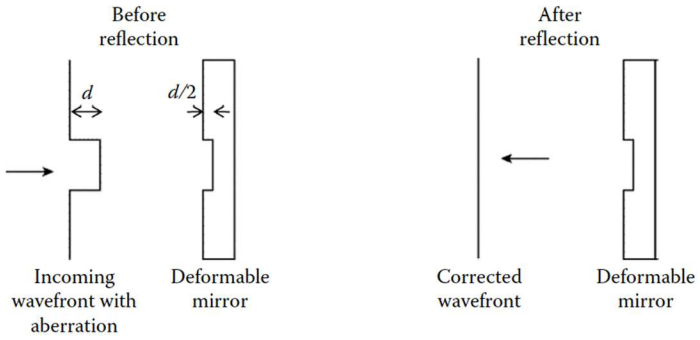

Figure 6: Wavefront correction with a deformable mirror. Adapted from [1].

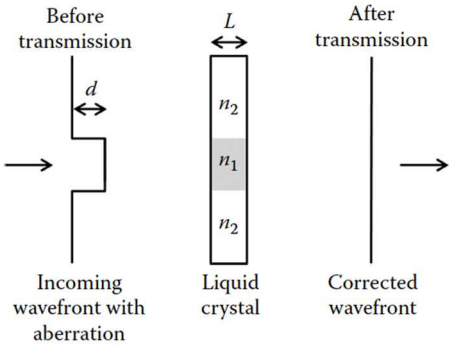

Figure 7: Wavefront correction with a spatial light modulator. Adapted from [1].

For a deformable mirror (Figure 6), the aberrated wavefront hits onto the surface of a deformable mirror. The reflected wavefront is corrected by reshaping the surface of the mirror to be conjugate to the wavefront distortion. For a spatial light modulator

(Figure 7), the propagation of the leading parts of the distorted wavefront is slowed down by changing the index of refraction within the modulator. The trailing parts are then aligned with the leading parts, so that the aberration compensation is implemented. These two types of wavefront correctors are compared in Table 1.

Table 1: Comparison between a deformable mirror and a spatial light modulator

Deformable Mirror	Spatial Light Modulator
Wavelength and polarization independent	Wavelength and polarization dependent
Correct low-order wavefront aberration	Correct low amplitude, high-order wavefront aberration
Refresh rate is several kilohertz	Refresh rate is about 100 Hz

1.4.2 Wavefront sensors

The common type of a wavefront sensor used in adaptive optics is the Shack-Hartmann sensor. In the Shack–Hartmann sensor, an array of lenslets collects light and images onto the detector plane (Figure 8). For each lenslet, the local gradient of the wavefront is calculated by measuring the lateral shift of the focus on the detector array (For a flat wavefront, every local lenslet focuses light onto the center of a detector pitch). From the local gradient measurements, the whole phase distribution can be constructed.

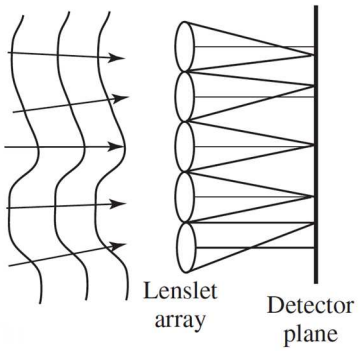

Figure 8: The Shack-Hartmann wavefront sensor. Adapted from [1].

1.5 Adaptive Optics in Microscopy

Commercial availability of adaptive optical elements has broadened the application of adaptive optics. Adaptive optics has been successfully incorporated in various types of microscopy to restore and enhance the image quality [22-24]. However, the implementation of adaptive optics in microscopy slightly differs from astronomy. As mentioned before, the system requires a reference point to directly measure wavefront aberration. This problem can be solved by injecting exogenous fluorescent beads into the sample to create "guide stars" [25], however, this method perturbs morphology of the sample. Another problem arises from the fact that a wavefront sensor cannot discriminate out-of-focus signals; thus, it cannot properly measure the wavefront. One of the solutions is utilizing the confocal principle for depth selection, but this method suffers from signal loss due to scattering which prevents the wavefront sensor from effectively collecting signals from the focal plane [26]. Instead, the most common

method to optimize the microscopic imaging systems, called an image-based "sensorless" approach, is correcting the aberrations by improving a certain image metric without a wavefront sensor [2]. Therefore, the successful application of "sensorless" adaptive optics depends on accurate selections of the control basis to control a wavefront corrector, the optimization algorithm and the optimization metric.

1.5.1 The representation of the control basis

Let us consider the control basis which is used to represent the wavefront corrector surface shape. The most convenient mathematical representation is Zernike polynomials which are an infinite set of orthonormal modes defined over the unit circle. Zernike polynomials are defined in polar coordinates (ρ, θ) as:

$$Z_{n,m} = \begin{cases} N_{n,m} R_{n,m} cosm\theta, & if\ m \geq 0 \\ N_{n,m} R_{n,m} sinm\theta, & if\ m\ < 0 \end{cases}$$

where n is a term order, $n - m$ must be even and the radial components $R_{n,m}(\rho)$ defined as:

$$R_{n,m}(\rho) = \sum_{s=0}^{\frac{n-|m|}{2}} \frac{(-1)^s\big((n-s)!\big)}{s!\left(\frac{(n+|m|)}{2} - s\right)!\left(\frac{n-|m|}{2} - s\right)!} \rho^{n-2s}$$

where a normalization factor $N_{n,m}$ according to Noll notation [27]:

$$N_{n,m} = \sqrt{\frac{2(n+1)}{1+\delta_{n,m}}}$$

Zernike polynomials are commonly used to represent optical aberrations since the low order terms define the classical aberrations, such as astigmatism, coma etc. Also, the lowest terms, namely tip ($n = 1, m = 1$), tilt ($n = 1, m = -1$) and defocus ($n = 2, m = 0$), describe the geometrical distortion and introduce a shift in x, y, z directions (Equation (2)). These terms have no effect on signal intensity. Therefore, they do not compromise the optical resolution and can be excluded from the control basis set. Moreover, it was demonstrated that a few orders of Zernike Polynomial have an effect on the degradation of image contrast in microscopy [28]; thus, a truncated set of the polynomials can represent the control basis set.

1.5.2 The optimization algorithm

There are different optimization approaches to implement adaptive optics in microscopy. The simplest one is the exhaustive or the brute force search, testing all possible combinations of control basis coefficients and finding the optimum one. However, this approach is time-consuming and practically unacceptable for imaging studies. There are other iterative methods, such as random search, hill-climbing [29], stochastic parallel descent [30] or genetic algorithms [31], which are more efficient and successfully applied in microscopy. These methods do not require a *priori* knowledge of how the image metric depends on aberration. Therefore, these approaches can lead to extensive light exposure of the sample which is undesirable for imaging studies.

By contrast, a different optimization method can be implemented based on the mathematical approximation of the image metric. For small aberrations, the image metric, a function with respect to aberration coefficients, can be expanded by the Taylor series up to a second-order near the aberration-free point [32]. Therefore, the quadratic maximization algorithm can be applied to estimate the aberration induced in the system. The principle of this algorithm is shown in Figure 9 and works as follows:

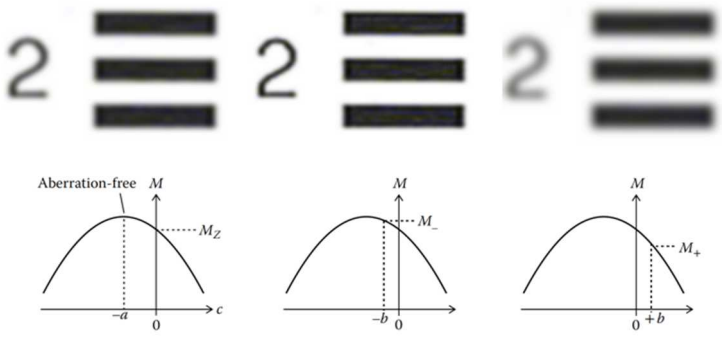

Figure 9: Principle of small aberration correction. Three images are obtained with applied bias aberrations 0, $-b$ and $+b$. The corresponding metric values M_z, M_- and M_+ are calculated from the images to calculate the correction amplitude a_i.

Suppose, N modes were chosen as the control basis. For the mode i, a positive bias, b, is applied and an image is acquired. Next, a negative bias with the same amplitude is applied and the image metric is measured. Finally, an image with no bias is obtained and the image metric is calculated. For the given mode, the correction amplitude a_i is determined using following equation:

$$a_i = \frac{b(M_+ - M_-)}{2M_+ - 4M_z + 2M_-}$$

where M_+, M_- and M_z are the image metrics for the positive, negative and no bias cases, respectively. The same routine is repeated for each mode and the correction amplitudes are calculated.

Another method of a "sensorless" approach is "pupil segmentation" as applied in two-photon microscopy [23]. The method is implemented by dividing the aberrated wavefront into segments. In a similar fashion, as in the Shack-Hartmann wavefront sensor, the gradient of the wavefront of the segment is calculated using image shift when local wavefront tilt is applied to the given segment. Gathering information of each segment, we can construct the whole phase function across the pupil and compensate aberration in the system.

1.5.3. The optimization metric

There are several types of the optimization metrics and the choice of the metric depends on the imaging properties of the microscope. The crucial points of selection are noise and photobleaching and the selection must be robust against these two parameters. For example, the total intensity can be suitable for CARS imaging [33], but cannot be for conventional fluorescence microscopy due to photobleaching. John Girkin compared five different metrics (Table 2) by imaging a thick mouse backskin tissue stained with hematoxylin and eosin [34]. Some of these metrics requires preprocessing

of the image, such as Fourier filter metric (Fourier transform $\mathfrak{F}$), Sobel filter metric (the convolution with Sobel kernels Sob_x and Sob_y) and wavelet filter metric (two-dimensional wavelet transform as in [35], where $LH(x, y)$ indicates applying a low-pass filter to the row of the image followed by a high-pass filter to the column of the image). Other two metrics do not require preprocessing (intensity squared metric and image variance metric).

The result revealed that the overall improvement in image quality and visual sharpness was comparable for all the metrics. No significant difference was observed in image contrast between the metrics. For each metric, the optimization led to the same combination of the Zernike terms to compensate the aberration as shown in Figure 10. As a result, the intensity squared metric or the image variance can be used as a valid optimization metric for adaptive optics in multiphoton microscopy since they do not require preprocessing of the image.

Table 2: Used metrics. $I(x, y)$ is the intensity of the $(x, y)^{th}$ pixel. Adapted from [1].

Metric Name	Analytical Formulation
Intensity Squared	$\frac{\sum_{pixels} I^2(x,y)}{(\sum_{pixels} I(x,y))^2}$
Image Variance	$\frac{\sqrt{\frac{1}{N}\sum_{pixels}(I(x,y)-< I >)^2}}{\sum_{pixels} I(x,y)}$
Fourier Filter	$\frac{\sum_{pixels}\lvert\Im\{I(x,y)\}\rvert_{masked}}{\sum_{pixels}\lvert\Im\{I(x,y)\}\rvert_{unmasked}}$
Sobel Filter	$\frac{\sum_{pixels}\sqrt{(Sob_x * I)^2(x,y) + \left(Sob_y * I\right)^2(x,y)}}{\sum_{pixels} I(x,y)}$
Wavelet Filter	$\sqrt{\frac{\left(\sum_{pixels} LH(x,y)^2 + \sum_{pixels} HL(x,y)^2\right)}{\sum_{pixels} I(x,y)^2 - \left(\sum_{pixels} LH(x,y)^2 + \sum_{pixels} HL(x,y)^2\right)}}$

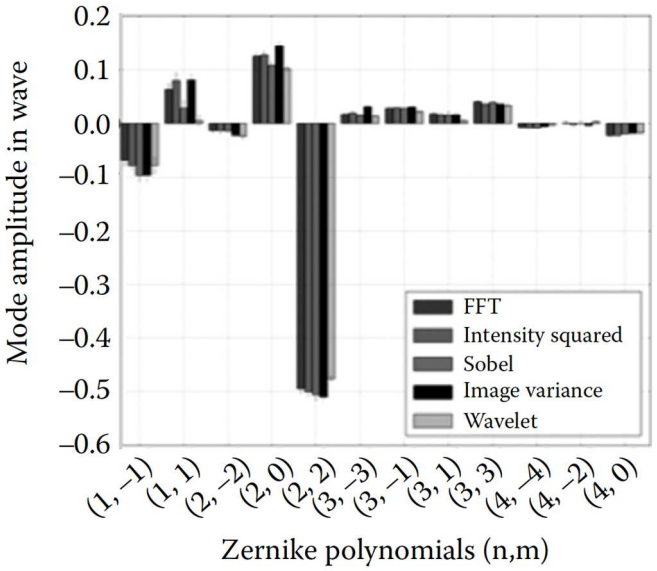

Figure 10: Zernike terms amplitude for the metrics. Adapted from [1].

2. Methodology

2.1 Experimental Setup

A schematic of the experimental setup is shown in Figure 11.

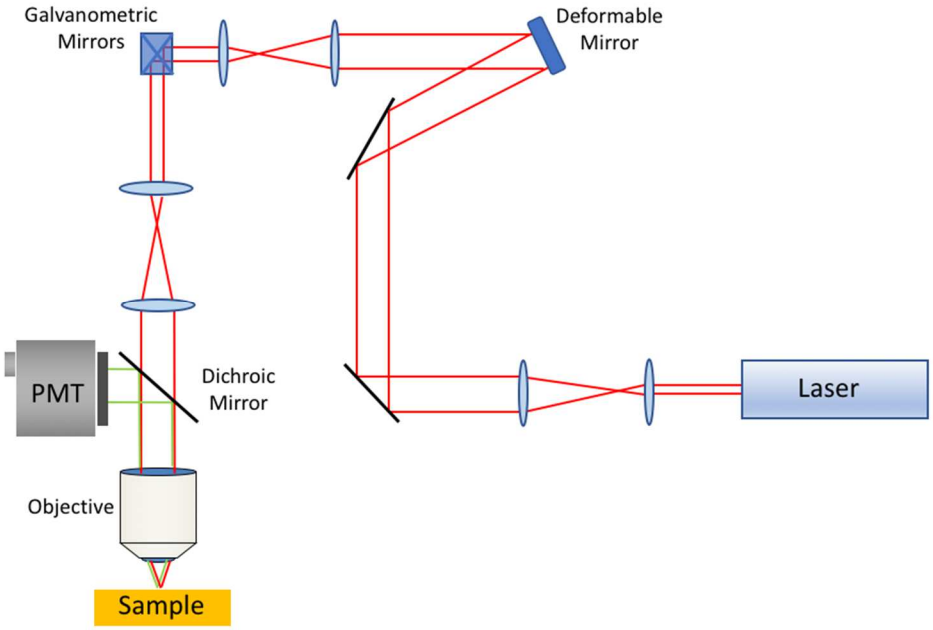

Figure 11: Experimental setup

A Ti:Sapphire modelocked laser (Coherent Chameleon, 80 MHz repetition rate) was used as the excitation beam at 817 nm. A portion of the laser beam is coupled into an optical parametric oscillator (OPO) (Coherent Mira-OPO) to generate a beam for the experiment at 720 nm. For both colors, the beam expanded and sent into a deformable mirror (Mirao 52e, Imagine Optics). Reflected light is sent to scanning galvanometric mirrors (Cambridge Corporation) and the beam was focused onto the sample with a 20x

air objective (Zeiss NA 0.80). The pupil planes of the deformable mirror, the galvanometric mirrors and the back aperture of the microscope objective were conjugated. The fluorescence signal from the sample is reflected via a dichroic mirror (Semrock FF662 long-pass) and collected with a photomultiplier tube (Hamamatsu R3896).

2.2 Samples

For all experiments, fluorescent YG microspheres (Polyscience Inc., USA) were used as the imaging target. These microspheres were imaged at 720 nm and 817 nm since they have a two-photon excitation signal for both colors.

To measure the point-spread function for each color, fluorescent YG microspheres of 0.2 um diameter were used. The microspheres were embedded in agarose gel. The agarose gel was sandwiched between two glass coverslips. Separation distance was approximately 150 μm between the coverslips.

For depth imaging, microspheres with diameter of 25 μm were used. The microspheres were also embedded in agarose gel with separation thickness of approximately 400 μm.

2.3 Adaptive Optics System

15 mm diameter deformable mirror (Mirao 52e, Imagine Optics) with 52 magnetic actuators was used to implement adaptive optics in the system. The position of

each actuator is controlled by applying a voltage between -1V and 1V, although sum of the absolute voltage value of all actuators are restricted not to exceed 25 V. This deformable mirror provides large dynamic range to compensate aberration comparing with other mirrors on the market [36]. Diameter of the beams was expanded approximately to 14 mm to eliminate the edge effect of the deformable mirror. First 11 modes of Zernike Polynomials (up to $n = 4$) were used as the control basis of the deformable mirror excluding piston, tip/tilt and defocus terms to avoid axial and lateral shift of the image. Sum of the squared pixel intensities of an image was used as the optimization metric. The quadratic maximization algorithm was selected as the optimization algorithm to correct the aberration. Additional iteration was performed to check the convergence of the optimization. The system is controlled using a custom-written program on LabWindows. All acquired data was processed and analyzed with MATLAB.

3. Results

3.1 Point Spread Function Measurement

To test adaptive optics in the system, the optical resolution of the microscope was measured before and after applying adaptive optics for each color. The optical resolution was defined as the full width at half maximum (FWHM) of the fitted Gaussian function to the intensity distribution of a single fluorescent microsphere with a diameter of 0.2 μm.

Table 3 shows the results of the corrected and uncorrected axial and lateral resolution of the system. At 720 nm, the axial and lateral resolutions were improved by 21.7% and 10.1%, respectively. On the other hand, the axial resolution was improved by 6.4% and the lateral resolution was improved by 16.5% for the excitation at 817 nm. However, the experimental results were not close to the theoretical values. The reason is that the back aperture of the objective was underfilled; thus, the effective numerical aperture of the objective was smaller than the given by the manufacturer. The experimental results suggest that the effective numerical aperture was 0.49 which was consistent with the value 0.55, calculated for the given beam size at the back aperture of the objective.

Table 3: Experimental and Theoretical Values of PSF FWHM for the Objective (NA=0.80) with AO on/off for excitation at 720 nm and 817 nm

Wavelength $\lambda\ (nm)$	Lateral Resolution			Axial Resolution		
	Experimental Value		Theoretical Value	Experimental Value		Theoretical Value
	AO off	AO on		AO off	AO on	
720	0.613 μm	0.551 μm	0.338 μm	4.47 μm	3.50 μm	1.13 μm
817	0.658 μm	0.616 μm	0.383 μm	5.03 μm	4.20 μm	1.28 μm

Figure 12 shows the amplitude values of the Zernike terms for the excitation at 720 nm and 817 nm. For both beams, the aberrations were predominated by different modes than spherical term which might be explained by slight off-axis misalignments of lenses in the beam path. As expected, two colors are affected by different amount of the aberration due to the different beam path configurations. The shape of the deformable mirror for each optimization is shown in Figure 13 and no significant difference can be seen. The reason is that the aberration amplitudes are small. Thus, our assumption for small aberration is satisfied.

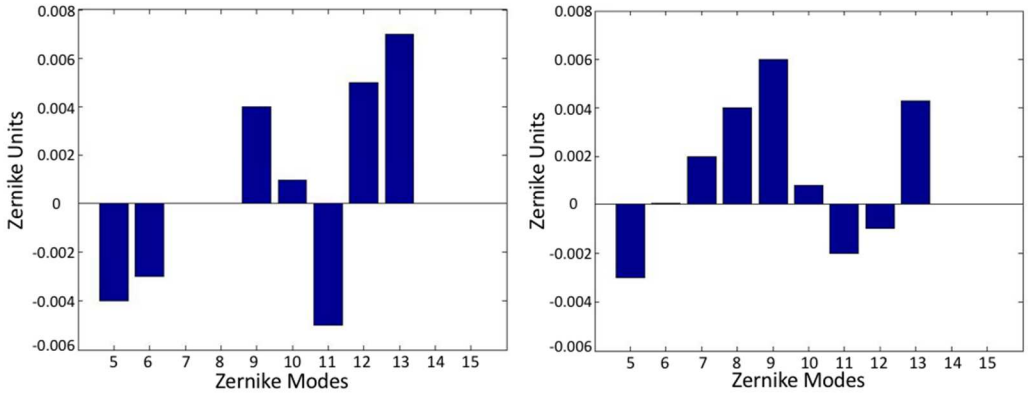

Figure 12: Zernike amplitude for excitation (left) at 720 nm and (right) at 817 nm.

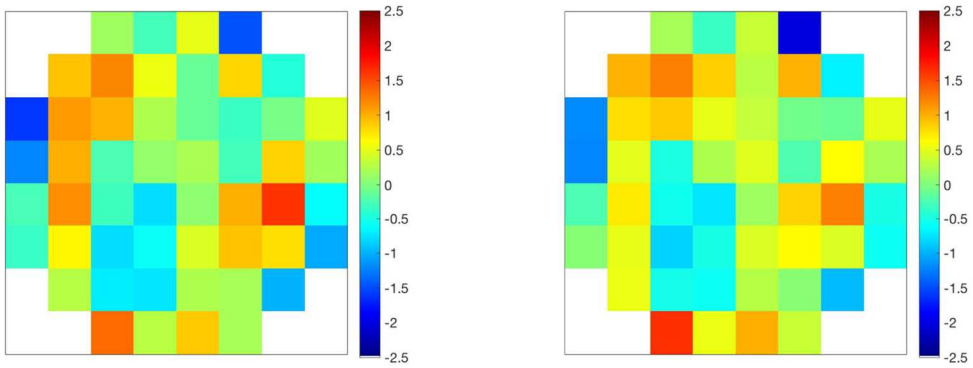

Figure 13: Deformable mirror shape for excitation (left) at 720 nm and (right) at 817 nm. The scale bars represent deformation in microns.

3.2 Imaging as a function of depth

In this experiment, the performance of adaptive optics was demonstrated at different depths in two-photon excitation microscopy. Twenty arbitrarily selected microspheres at different depths were served as the evaluation metric to compare the optimization as a function of imaging depth. The optimization metric was calculated

with an image of a single bead over the field of view of 40 x 40 μm.

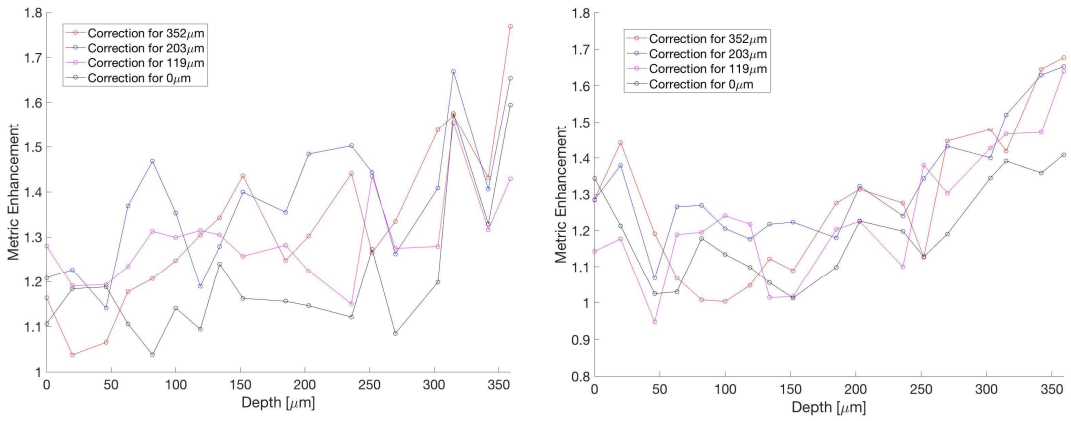

Figure 14: Metric enhancement vs penetration depth. Excitation wavelength (left) 720 nm and (right) 817 nm.

The aberration compensation was performed to obtain the optimized mirror-shape at depth 0 μm, 119 μm, 203 μm and 352 μm. Z-stack data was collected for each mirror-shape including uncorrected one. Figure 14 shows the metric enhancement, calculated by dividing the corrected metric by the uncorrected metric, as a function of depth for each optimization at 720 nm and 817 nm. As can been seen, the adaptive optics correction produces greater improvement with increasing imaging depth. The maximum signal improvements of 77% and 68% are obtained for excitation at 720 nm and 817 nm, respectively. Another notable result is that the optimization for each color produces different enhancement factor which might be caused by the large system aberration comparing to the sample-induced aberration.

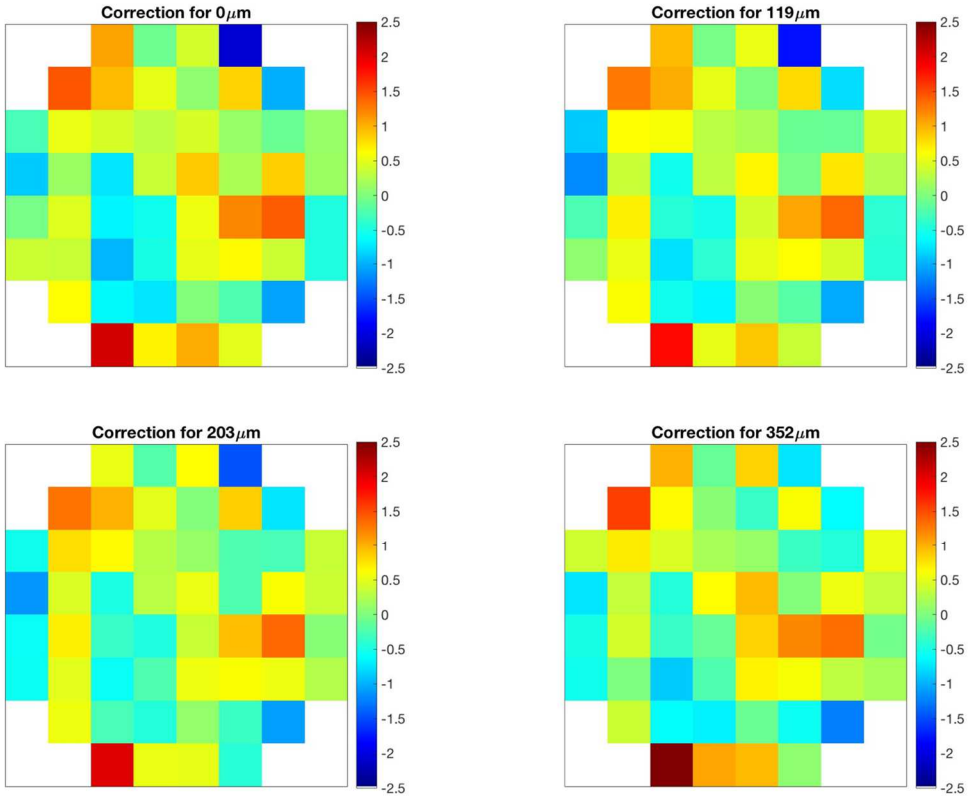

Figure 15: Deformable mirror shape at different depth. Excitation wavelength is 720 nm. The scale bars represent deformation in microns.

Figure 15 and 16 show the deformable mirror-shape for each optimized depth. The result supports the assumption on homogeneity of the aberration since the mirror-shape slightly differs. The amplitude of Zernike terms varies as a function of depth (Figure 17 and 18) which indicates the increase in the sample-induced aberration. As expected, the higher order of the Zernike terms became more predominant as the imaging depth increased since these higher order terms correspond to higher spatial frequencies.

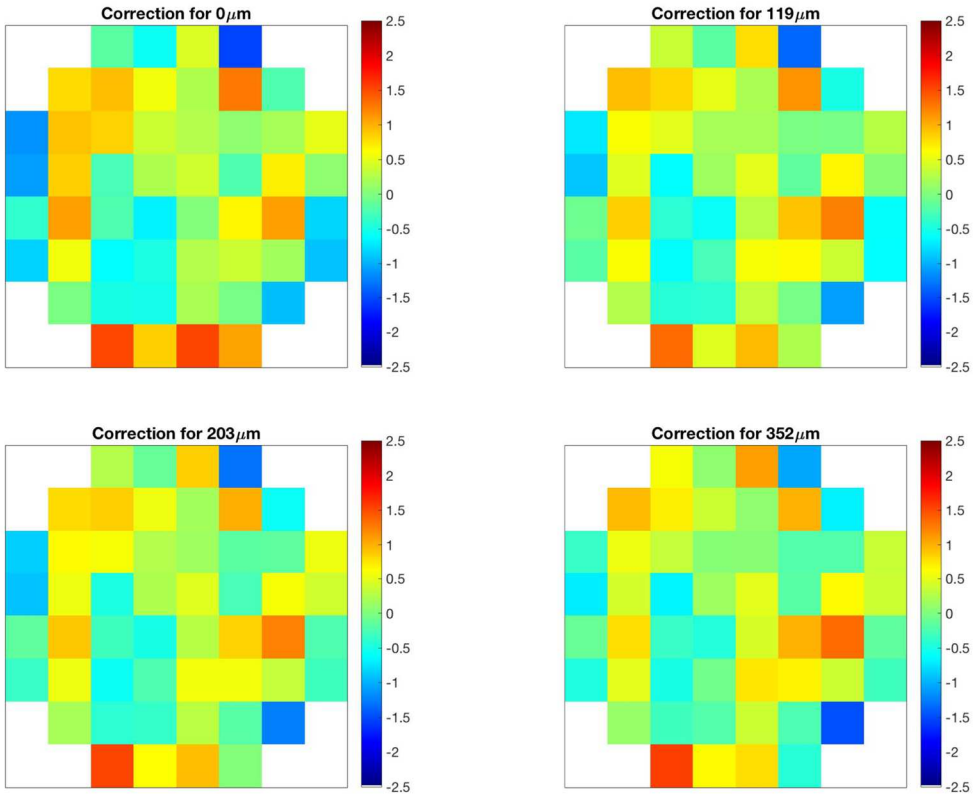

Figure 16: Deformable mirror shape at different depth. Excitation wavelength is 817 nm. The scale bars represent deformation in microns.

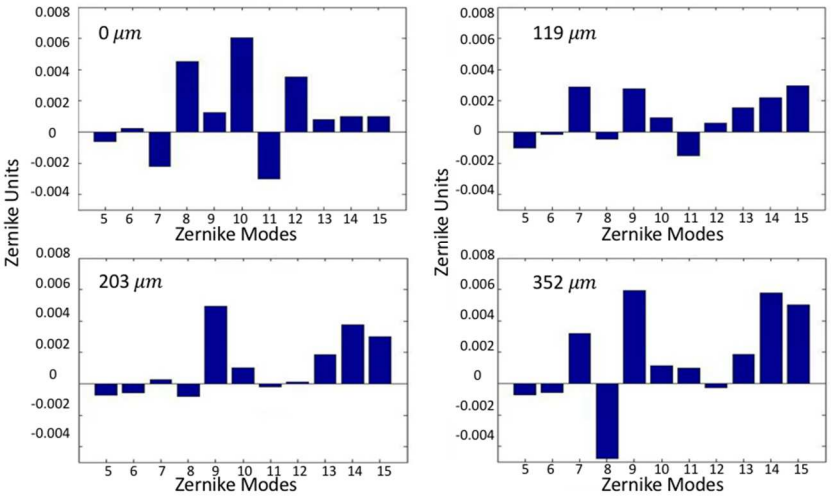

Figure 17: Zernike mode amplitude for excitation at 720 nm.

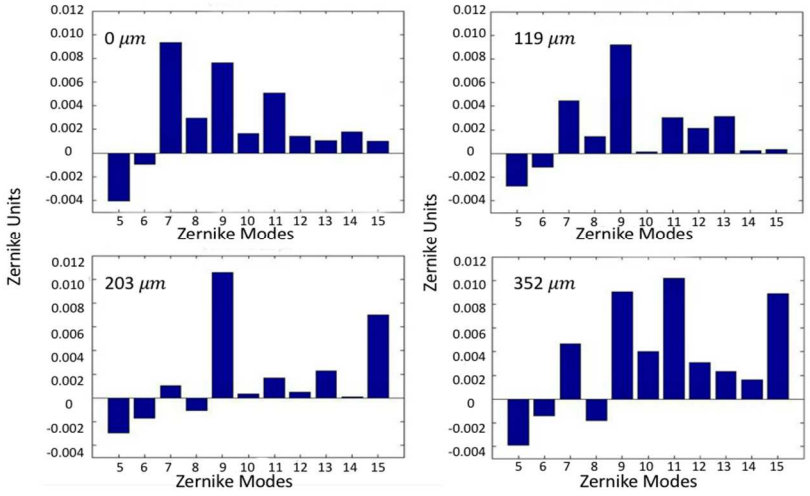

Figure 18: Zernike mode amplitude for excitation at 817 nm

4. Discussion

In this thesis, I presented the implementation of adaptive optics in multiphoton microscopy. The spatial resolution of the microscope was measured and improved using a deformable mirror for different excitation wavelengths. Furthermore, the optimization improvement was demonstrated as a function of depth. This study revealed that greater improvement is obtained as the imaging depth is increased.

For two-beam experiments, such as pump-probe imaging or CARS, adaptive optics can optimize the imaging focal spot for both colors. We can expect more improvement in the experiments since the detected signal is dependent on spatial overlap of two beams. Moreover, the implementation of adaptive optics provides a feasibility of reducing the beam intensity by keeping the same signal level which can be highly beneficial for sensitive imaging studies.

Nonetheless, it is important to discuss the limitations of adaptive optics in microscopy. First, the performance of adaptive optics depends on the sample under investigation. In my experiments, the optimization was followed by the assumption that the aberration is small and spatially homogeneous. Therefore, I used the optimization metric of an entire image of a single microsphere. For different samples, adaptive optics should be thoroughly implemented depending on the spatial variation of aberration. Therefore, different approaches can be applied. One of the methods can be using

conjugate adaptive optics when the pupil plane of a deformable mirror is conjugated to the aberration layer within the sample [37]. Conjugate adaptive optics provides better correction when the aberration is predominant by a specific region within the sample. An alternative approach is multiconjugate adaptive optics [38]. This method also implements the aberration compensation when the sample has predominant aberration layers. The basic idea behind multiconjugate adaptive optics is incorporating two or more deformable mirrors into the system and placing the mirrors conjugate to the predominant aberration layers within the sample. It was shown theoretically that multiconjugate method outperforms the adaptive optics configuration with a single correction device [38]. However, this approach is more complicated and more expensive to incorporate into the experimental setup.

The second limitation is scattering. It is well-known that scattering grows exponentially as imaging depth increases. One approach to reduce scattering is optical clearing. This method reduces scattering by decreasing the inhomogeneity within the sample when optical-clearing agents diffuse into the sample [39]. However, we must consider the effects of optical clearing agents on morphology and functionality of the sample before applying optical clearing. Therefore, the specimen should be investigated on a case by case basis to apply aforementioned methods to optimally configure the imaging system.

References:

1. Kubby, J.A., *Adaptive Optics for Biological Imaging*. 2013: CRC press.

2. Booth, M.J., *Adaptive optical microscopy: the ongoing quest for a perfect image.* Light: Science & Applications, 2014. **3**(4): p. e165.

3. Fischer, M.C., et al., *Invited Review Article: Pump-probe microscopy.* Review of Scientific Instruments, 2016. **87**(3): p. 031101.

4. Minsky, M., *Confocal scanning microscope.* Rapport technique, Patent, 1955. **3**.

5. Inoué, S., *Foundations of confocal scanned imaging in light microscopy*, in *Handbook of biological confocal microscopy*. 2006, Springer. p. 1-19.

6. Denk, W., J.H. Strickler, and W.W. Webb, *Two-photon laser scanning fluorescence microscopy.* Science, 1990. **248**(4951): p. 73-76.

7. Freund, I. and M. Deutsch, *Second-harmonic microscopy of biological tissue.* Optics letters, 1986. **11**(2): p. 94-96.

8. Guo, Y., et al., *Second-harmonic tomography of tissues.* Optics Letters, 1997. **22**(17): p. 1323-1325.

9. Barad, Y., et al., *Nonlinear scanning laser microscopy by third harmonic generation.* Applied Physics Letters, 1997. **70**(8): p. 922-924.

10. Squier, J.A., et al., *Third harmonic generation microscopy.* Optics express, 1998. **3**(9): p. 315-324.

11. Cheng, J.-X. and X.S. Xie, *Coherent anti-Stokes Raman scattering microscopy: instrumentation, theory, and applications*. 2004, ACS Publications.

12. Mohler, W., A.C. Millard, and P.J. Campagnola, *Second harmonic generation imaging of endogenous structural proteins.* Methods, 2003. **29**(1): p. 97-109.

13. Dombeck, D.A., et al., *Uniform polarity microtubule assemblies imaged in native brain tissue by second-harmonic generation microscopy.* Proceedings of the National Academy of Sciences, 2003. **100**(12): p. 7081-7086.

14. Gualda, E.J., et al., *Third-harmonic generation and multi-photon excitation fluorescence imaging microscopy techniques for online art conservation diagnosis.* Applied spectroscopy, 2009. **63**(3): p. 280-285.

15. Fu, D., et al., *High-resolution in vivo imaging of blood vessels without labeling.* Optics Letters, 2007. **32**(18): p. 2641-2643.

16. Matthews, T.E., et al., *Pump-Probe Imaging Differentiates Melanoma from Melanocytic Nevi.* Science Translational Medicine, 2011. **3**(71): p. 71ra15-71ra15.

17. Villafana, T.E., et al., *Femtosecond pump-probe microscopy generates virtual cross-sections in historic artwork.* Proceedings of the National Academy of Sciences, 2014. **111**(5): p. 1708-1713.

18. Goodman, J.W., *Introduction to Fourier optics*. 2005: Roberts and Company Publishers.

19. Keller, H.E., *Objective lenses for confocal microscopy*, in *Handbook of biological confocal microscopy*. 2006, Springer. p. 145-161.

20. Hardy, J.W., *Adaptive optics for astronomical telescopes*. 1998: Oxford University Press on Demand.

21. Babcock, H.W., *The possibility of compensating astronomical seeing.* Publications of the Astronomical Society of the Pacific, 1953. **65**(386): p. 229-236.

22. Booth, M.J., et al., *Adaptive aberration correction in a confocal microscope.* Proceedings of the National Academy of Sciences, 2002. **99**(9): p. 5788-5792.

23. Ji, N., D.E. Milkie, and E. Betzig, *Adaptive optics via pupil segmentation for high-resolution imaging in biological tissues.* Nat Meth, 2010. **7**(2): p. 141-147.

24. Débarre, D., et al., *Image-based adaptive optics for two-photon microscopy.* Optics letters, 2009. **34**(16): p. 2495-2497.

25. Tao, X., et al. *Adaptive optics confocal fluorescence microscopy with direct wavefront sensing for brain tissue imaging*. in *SPIE MOEMS-MEMS*. 2011. International Society for Optics and Photonics.

26. Cha, J.W., J. Ballesta, and P.T. So, *Shack-Hartmann wavefront-sensor-based adaptive optics system for multiphoton microscopy.* Journal of biomedical optics, 2010. **15**(4): p. 046022-046022-10.

27. Noll, R.J., *Zernike polynomials and atmospheric turbulence.* JOsA, 1976. **66**(3): p. 207-211.

28. Schwertner, M., M. Booth, and T. Wilson, *Characterizing specimen induced aberrations for high NA adaptive optical microscopy.* Optics express, 2004. **12**(26): p. 6540-6552.

29. Wright, A.J., et al., *Exploration of the optimisation algorithms used in the implementation of adaptive optics in confocal and multiphoton microscopy.* Microscopy Research and Technique, 2005. **67**(1): p. 36-44.

30. Vorontsov, M. and V. Sivokon, *Stochastic parallel-gradient-descent technique for high-resolution wave-front phase-distortion correction.* JOSA A, 1998. **15**(10): p. 2745-2758.

31. Man, K.-F., et al., *Genetic Algorithms: Concepts and Designs with Disk.* 1999.

32. Booth, M.J., *Wave front sensor-less adaptive optics: a model-based approach using sphere packings.* Optics express, 2006. **14**(4): p. 1339-1352.

33. Wright, A., et al., *Adaptive optics for enhanced signal in CARS microscopy.* Optics express, 2007. **15**(26): p. 18209-18219.

34. Girkin, J.M., S. Poland, and A.J. Wright, *Adaptive optics for deeper imaging of biological samples.* Current opinion in biotechnology, 2009. **20**(1): p. 106-110.

35. Kautsky, J., et al., *A new wavelet-based measure of image focus.* Pattern recognition letters, 2002. **23**(14): p. 1785-1794.

36. Fernández, E.J., et al., *Adaptive optics with a magnetic deformable mirror: applications in the human eye.* Optics Express, 2006. **14**(20): p. 8900-8917.

37. Mertz, J., H. Paudel, and T.G. Bifano, *Field of view advantage of conjugate adaptive optics in microscopy applications.* Applied optics, 2015. **54**(11): p. 3498-3506.

38. Simmonds, R.D. and M.J. Booth, *Modelling of multi-conjugate adaptive optics for spatially variant aberrations in microscopy.* Journal of Optics, 2013. **15**(9): p. 094010.

39. Tuchin, V.V., *Optical clearing of tissues and blood using the immersion method.* Journal of Physics D: Applied Physics, 2005. **38**(15): p. 2497.